UNIVERSITÀ DEGLI STUDI DI PADOVA

Dipartimento di Ingegneria Industriale DII

Corso di Laurea Magistrale in Ingegneria Aerospaziale

TESI DI LAUREA MAGISTRALE

Comparison of fragments generated by hypervelocity impacts on aluminium and composite targets

Relatore
Dr. Lorenzo Olivieri
Correlatore
Dr. Francesco Fabri

Laureando: *Alessio Vianello*
Matricola: 2130743

ANNO ACCADEMICO 2025/2026

A chi è sempre stato al mio fianco,
e continuerà ad esserlo.

Abstract

The evolution of space debris over time is currently being monitored with great attention by space agencies such as NASA and ESA, as well as by private companies entering the space sector. The main issue concerns the possibility of collisions between orbital debris and other objects in space. In Low Earth Orbit (LEO), these impacts can occur at speeds of several *km/s*, potentially leading to the complete destruction of the objects involved. Characterization of debris generation following an impact is fundamental for studying the long-term evolution of the space debris environment. Since direct observation of on-orbit collisions is limited, hypervelocity impact tests conducted in laboratory facilities are essential to collect data about the fragmentation process and develop break-up models. Modern satellites employ advanced structural configurations and new materials, such as aluminum honeycomb panels and carbon-fiber-reinforced composite plates (CFRPs). In this context, several hypervelocity impact tests were carried out at the Hypervelocity Impact Facility of the University of Padova involving these new types of structural solutions. This thesis considers four impact experiments: two involving aluminum honeycomb panels and two involving CFRPs. The analysis presents the shape distributions, the characteristic length cumulative distribution, and the area-to-mass ratio of the fragments collected in such tests. The results are then compared, highlighting the difference between the two materials, showing that CFRPs strongly differ from aluminum honeycomb panels in terms of size, shape, and number of the generated fragments.

Keywords: Debris, Fragments, Hypervelocity, Aluminium, CFRP

Sommario

La crescita dei detriti spaziali nel corso degli anni è monitorata con attenzione dalle principali agenzie spaziali, come NASA ed ESA, e dalle aziende private che operano nel settore spaziale. La principale preoccupazione riguarda la possibilità di collisione tra tali detriti e altri oggetti in orbita. Nelle orbite terrestri basse (LEO) tali impatti possono avvenire a velocità di svariati *km/s*, e possono comportare una completa distruzione degli oggetti coinvolti. Riuscire a caratterizzare il processo di generazione dei detriti a seguito di un impatto è fondamentale per studiare l'evoluzione dell'ambiente detritico. Poiché l'osservazione diretta di collisioni orbitali è complessa, i test di ipervelocità condotti in laboratorio sono fondamentali per raccogliere dati riguardo i meccanismi di frammentazione e sviluppare modelli analitici di tali fenomeni. I satelliti più moderni utilizzano nuove configurazioni strutturali e nuovi materiali, ad esempio pannelli honeycomb in alluminio o lastre di materiale composito in fibra di carbonio (CFRPs). A tal riguardo, nel Laboratorio di Ipervelocità dell'Università di Padova sono stati condotti vari test su tali soluzioni strutturali. In questa tesi vengono considerati quattro di questi esperimenti: due condotti su pannelli honeycomb di alluminio e due su materiale composito. L'analisi condotta fornisce informazioni su forma, lunghezza caratteristica e rapporto di area su massa dei frammenti provenienti dai vari tests. Infine, i risultati sono confrontati per evidenziare le differenze tra i due tipi di materiali, in particolare è stato osservato che i frammenti in composito differiscono da quelli provenienti dai pannelli honeycomb in alluminio per forma, numero e dimensione.

Acknowledgements

Come prima cosa vorrei ringraziare il mio relatore, Lorenzo Olivieri, per questa esperienza. Poter finalmente vedere e lavorare con mano su cose studiate in questi cinque anni è davvero indescrivibile. Lo ringrazio, inoltre e soprattutto, per la sua infinita disponibilità e i suoi consigli che sono stati fondamentali per questo risultato. Voglio ringraziare inoltre Francesco e Marco che mi hanno affiancato durante l'attività sperimentale, alternando professionalità e momenti di gioco. Ho trovato veramente un bel clima di lavoro e mi sono davvero divertito durante questi mesi passati insieme. Mi mancheranno i magici caffè preparati sul fornello del laboratorio. Chi non ringrazio sono invece la bilancia e i centinaia di frammenti che ho dovuto pesare. Visto il tema di questa tesi, è proprio il caso di dirlo: *"What a piece of junk!"* [Luke Skywalker, *Star Wars: A New Hope].*

Ringrazio di cuore la mia famiglia, Mamma e Papà, per avermi sempre sostenuto giorno dopo giorno, senza di loro tutto questo non sarebbe stato possibile. Ringrazio anche le mie nonne, i miei zii, zie, cugini che mi hanno sempre incoraggiato con affetto e ammirazione. E ringrazio anche chi oggi non c'è più, ma ha sempre creduto in me.
Un grazie particolare va inoltre a tutti i miei amici. Avete reso questi anni molto più sereni e divertenti, non sarebbe stato davvero lo stesso senza di voi. E sono certo che a tutti i bei momenti che abbiamo passato insieme se ne aggiungeranno sempre di nuovi e ancora più epici.
Tutti voi siete la mia Forza, vi voglio bene.

E infine, vorrei ringraziare me stesso per essere arrivato fino a qui, superando le difficoltà. *"Well, I wasn't gonna let you all the credit and take all the reward."* [Han Solo, *Star Wars: A New Hope*]. Sì, come avrete capito, sono un grande fan di Star Wars e se c'è una frase che veramente mi è rimasta dentro come un mantra è: *"Do, or do not. There is no try."* [Yoda, *Star Wars: The Empire Strikes Back*]. Io ho scelto Do, Fare, perchè il primo passo per raggiungere un obbiettivo è avere la volontà di raggiungerlo e crederci fino infondo. *"In my experience, there's no such thing as luck."* [Obi-Wan Kenobi, *Star Wars: A New Hope*]. La fortuna e il caso non esistono, tutto viene da impegno e sacrificio: *"Your focus determines your reality."* [Qui-Gon Jinn, *Star Wars: The Phantom Menace*].

E ora che ho concluso tutto, un nuovo capitolo avrà inizio. *"This is where the fun begins!"* [Anakin Skywalker, *Star Wars: Revenge of the Sith*].

"May the Force be with You"

Contents

List of Figures

List of Figures

List of Tables

List of Tables

List of Symbols

a	largest dimension of the object
b	second largest dimension of the object
c	smallest dimension of the object
L_c	characteristic length
m	mass of the single fragment
v	impact velocity
t	target thickness
M_{TARG}	mass of the target
m_{COLL}	total mass of the collected fragments
m_{PROJ}	mass of the projectile
A	cross sectional area of the fragment
A/m	area-to-mass ratio
η	efficiency in mass collection
σ	variance
r^2	determination coefficient
RMSE	root mean square error

Subscripts

before	before the test
after	after the test

List of Acronyms

NASA	National Aeronautics and Space Administration
ESA	European Space Agency
LEO	Low Earth Orbit
CFRP	Carbon-Fiber-Reinforced composite Plate
IADC	Inter-Agency Space Debris Coordination Committee
EMR	Energy-to-Mass Ratio
CISAS	Center for Space Studies and Activities
LGG	Light-Gas Gun

1 Introduction

1.1 Space debris history and generation

The increase in space debris is currently one of the major problems affecting the satellites orbiting the Earth [1]. By the IADC definition [2], space debris are any man-made objects in orbit or re-entering the atmosphere with no control, thus they include expired spacecraft, fragments due to stage separation, breakups, collision or explosion, upper stages of used rockets, flecks of paint detached from objects, slag particles from solid propellant boosters. Everything we launch into space could become debris. The problem is that space junk could impact operative satellites, leading to catastrophic destruction or severe damage significantly affecting the lifespan of missions. The presence of debris in near-Earth orbits is a direct consequence of human activities in space [3]. Since the beginning of space exploration in 1957, when the first satellites successfully reached orbit, we have started generating debris, which tend to accumulate in orbit because they require several years to decay. Over the years, the number of satellites in space has drastically increased, and with them also the debris (Fig. 1) [4, 5].

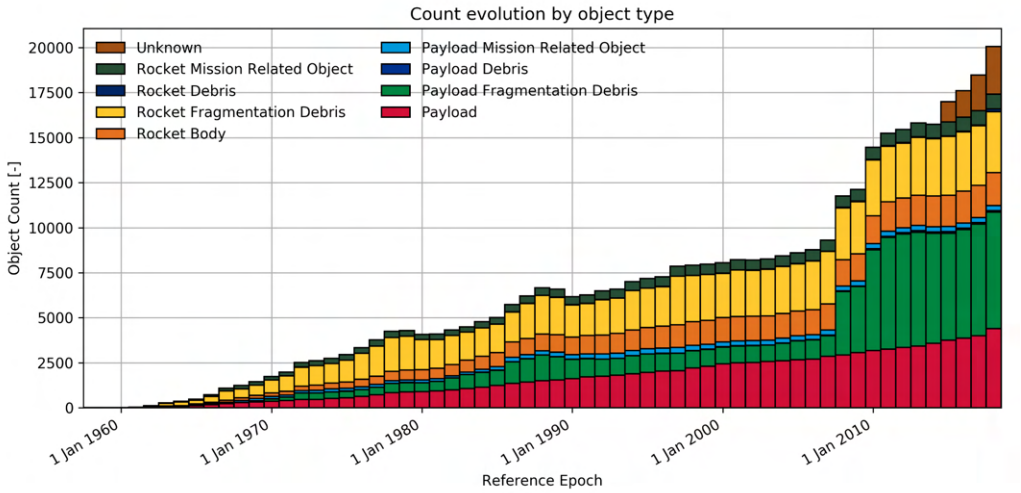

Figure 1: Evolution of orbital debris and their origin since the beginning of the space era. Source: https://www.sdo.esoc.esa.int

The production of space junk is directly related to the growth of space launches [6]. In fact, the first sources of debris are space missions themselves. Mission related objects such as defunct satellites, upper stages of launch vectors, ring adapters, fairings, fragments generated by stage separation, and aluminum oxide

(Al2O3) slag particles released by solid boosters contribute significantly to the debris population [7].

Another major source of debris consists of accidental explosions of satellites and rocket bodies, often due to leaks of propellant or system malfunctions. Such explosions can generate several thousand fragments from a single object, making them extremely hazardous. Besides that, unfortunately, some explosions are completely deliberate, such as the Chinese FengYun-1C antisatellite test in 2007 or Russia's COSMOS 1408 in 2021 [8, 9, 10, 11]. However, the most critical source of debris is the generation of fragments following orbital collisions [12, 13]. Impacts between two satellites or between satellites and existing debris can lead to a catastrophic destruction spreading thousands or even millions of fragments. A notable example occurred in 2009 with a collision between the American communications satellite Iridium-33 and the dismissed Russian Kosmos2251 military satellite [14].

The increase in space debris increases the probability of other future impacts leading to the generation of new fragments. This problem was presented for the first time in 1978 by NASA scientist Donald J. Kessler, and is referred to as Kessler syndrome [15]. The density of space debris in LEO will reach a critical level above which there will be an unpredictable chain of collisions exponentially increasing the number of debris over time. This catastrophic scenario could potentially prevent access to orbit for many generations, leading to dramatic consequences. According to Kessler himself, early evidence of this tragedy could already be seen [16].

In order to mitigate the risk, space agencies such as NASA and ESA are now pushing forward new international guidelines to limit orbital debris [17, 18]. However, in the near future, we can expect a further deterioration [19, 20] of the debris environment due to the continuous growth in commercial launches [21, 22, 23, 24, 25], including both small satellites [26] and large constellations [27, 28, 29].

Even the implementation of severe regulations could not be sufficient anymore, since if we even stop all future launches the number of debris is still expected to increase due to orbital collisions. The only way to address the problem seems to be active debris removal missions, which are now under study [30, 31, 32, 33].

1.2 Monitoring of debris environment

The debris environment is constantly monitored by space agencies such as ESA and NASA [34, 35], as it poses a significant risk to the survival of satellites in Earth orbit. The statistical model of ESA [36, 37] (MASTER-8, reference population 08/2024) estimates the following numbers of objects currently in orbit, subdivided by size class.

- 54000 space objects greater than 10 *cm* (including around 9300 active payloads).
- 1.2 million space debris objects from greater than 1 *cm* to 10 *cm*.
- 140 million space debris objects from greater than 1 *mm* to 1 *cm*.

Large objects are regularly tracked by Space Surveillance Networks [38, 39] which keep a record of about 44870 objects by January 2026. Unfortunately, even for this class size, not all objects are tracked and cataloged, representing a serious problem. In fact, a collision with such large debris would result in a complete destruction of the impacted satellites. For smaller size objects, the situation is even more critical since it is not even possible to track them individually. This necessitates reliance on statistical models for the impact probability [5, 36, 39, 40]. Despite the small size, an impact with those objects is still able to seriously damage one or more subsystems resulting in a mission failure. The only way to address this issue is implementing passive shielding techniques [41, 42].

1.3 Hypervelocity impact models

Space debris can reach velocities up to 16 *km/s* in LEO. Hypervelocity impacts on a target produce severe effects [43, 44], including surface craterization, high compression state, pressure waves in the material, drastic raise of temperature, phase transition and plasma ejections.
The damage strictly depends on size, mass and velocity of the impacting fragment. A relevant parameter is the energy-to-mass ratio (EMR) of the impact defined as shown in Eq.(1). Typically, if $EMR > 40$ *J/g* the collision leads to a catastrophic destruction of the impacted object.

$$EMR = \frac{\frac{1}{2} m_{PROJ} v^2}{M_{TARG} + m_{PROJ}} \tag{1}$$

However, in general, the effects of the impacts depend on materials, geometries, and impact parameters and can be harmful even for lower energy levels. For a given target, the survivability condition can be described using the Ballistic Limit Equation (BLE) [45]. The resulting curve in the d-v diagram represents, for each impact velocity v, the minimum size d of the impacting objects able to perforate the target (Fig. 2).

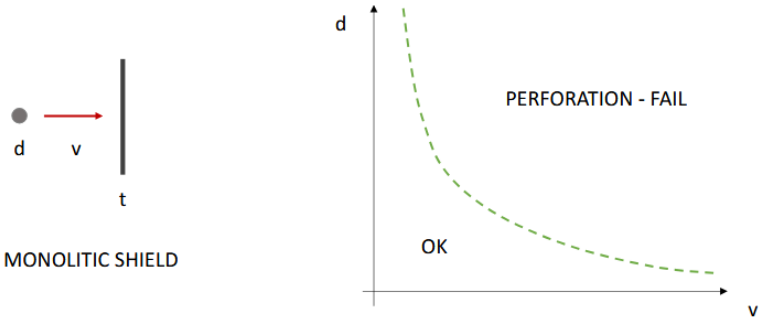

Figure 2: Example of a ballistic limit curve.

Due to their high velocity, even small debris can easily exceed the ballistic limit in case of collision with a target, generating a significant number of new debris. As space collisions involving debris are expected to become more frequent [4], it is important to develop accurate break-up models to study the generation of new fragments upon collisions [46, 47] in order to model the long-term evolution of the space debris environment [48]. To date, the most accurate fragmentation model is the NASA Standard Breakup Model (SBM) [49, 50]. The model uses the EMR to evaluate the severity of the collision and provide empirical relations to estimate the expected number, characteristic length, area-to-mass ratio of the generated fragments. The model was developed using fragmentation data collected by Space Surveillance Networks and ground experiments on mock-up satellites in hypervelocity facilities. Further ground tests involving new materials and satellite configurations are always essential to validate or improve current models [51] or develop new ones [52].

2 Ground-based hypervelocity tests

The validation of the NASA SBM model [49, 50] is based on the analysis of debris generation both from the observation of space fragmentation events [53, 54] and ground-based hypervelocity tests. Despite being the most reliable model available, several limitations are evident. The model is based on fragmentation data from old generations satellites that are no more representative of current state-of-the-art architectures. Modern spacecraft use different configurations and new materials.
In addition, fragments smaller than 1 cm are not well represented in the model since very few sets of data are available for this size. Most of them come from SOCIT laboratory tests data [55, 56], however, as shown by Hanada's tests, they are not well representative [57]. Moreover, the model does not account for fragment shape, fragmentation process, and impact geometry.
In this context, ground fragmentation tests are essential to improve current break-up models. Important tests were performed on large mock-up satellites, for example NASA's DebrisSat experiment [58] or Hanada's and Lan's experiments [57, 59, 60]. More recent tests also involved small satellites like Cubesat [61] or Picosat [62, 63], which are typical of the new space economy.
Hypervelocity tests on complete mock-up models provide more reliable data on satellite fragmentation processes, but require very advanced facilities and significant effort to collect and analyze results [64, 65].

2.1 Characterization of materials' fragmentation behaviour

Relevant data on fragment generation can also be obtained by performing hypervelocity impact tests on simple small elements like plates. These experiments are primarily useful for characterizing the fragmentation behavior of different materials. Many tests were already performed on aluminum plates considering different impact conditions [66, 67, 68, 69]. These results are extremely useful since aluminum remains the most widely used material in space applications. Despite this, with the rise of the new space economy, carbon-fiber-reinforced composite plates (CFRPs) are increasingly employed on modern satellites [70]. In literature some studies on CFRPs are already present, examining the ballistic limit equation, damage assessment, and fragment distribution [71, 72, 73, 74]. However, these works mainly focus on the CFRPs fragmentation behavior and do not provide a direct comparison with aluminum, which is the goal of this current study. Aluminum is an isotropic metallic material, while CFRPs consist of multiple layers of oriented fibers resulting in anisotropic behavior. Consequently, the fragmentation processes of these two materials are expected to differ significantly.

2.2 New hypervelocity tests performed by University of Padova

A new set of hypervelocity impacts tests on aluminium and composite plates was carried out at the Hypervelocity Impact Facility of the Center for Space Studies and Activities (CISAS) "Giuseppe Colombo" of the University of Padova [75] using a two-stage Light-Gas Gun (LGG) capable of accelerating projectiles up to 100 *mg* at a maximum speed of 5.5 *km/s* (Fig. 3).

Figure 3: Two-stage Light-Gas Gun at the Hypervelocity Impact Facility of the University of Padova.

Several tests were carried out; here in this work only four of them are presented: two tests on aluminum honeycomb panels (Test 9225 and Test 9235) and two tests on CFRP plates (Test 9222 and 9234). All tests were performed above the ballistic limit of the respective material, ensuring target perforation. Test 9225 and Test 9235 used as the target two aluminum honeycomb panels with thicknesses of 1" and 2", respectively, covered with aluminum skin (Fig. 4).

Both tests used aluminum (Al-1100) spherical projectiles with a diameter of 2.9 *mm* and a mass of 0.034 g. The projectiles were accelerated respectively to 4.71 *km/s* and 3.63 *km/s* impacting the target at 0° (normal incidence). In Test 9222 the target was a 100×100 mm^2 CFRP plate of 4 *mm* thickness, while Test 9234 employed a 100×100 mm^2 kevlar-reinforced CFRP plate of 3 *mm* thickness (Fig. 7). The projectiles in both cases were the same as in the previous tests. This time the shooting velocities were 3.49 *km/s* and 4.63 *km/s*, respectively, and the impact still occurred with an impact angle of 0°. The parameters of all tests are summarized in Table 1.

Test Code	***Type of target***	***Target mass [g]***	***Projectile size [mm]***	***Projectile mass [g]***	***Impact velocity [km/s]***
9225	2" honeycomb panel + Al skins	81.709	2.9	0.034	4.71
9235	1" honeycomb panel + Al skins	30.422	2.9	0.034	3.63
9222	100×100 mm^2 CFRP thickness 4 mm	102.867	2.9	0.034	3.49
9234	100×100 mm^2 CFRP thickness 3 mm + Kevlar layer	83.639	2.9	0.034	4.63

Table 1: Characterization of the targets, projectile and main impact parameters used in the impact tests.

In order to simplify fragment collections after the impact, a dedicated set-up was realized, taking as reference the one used by Nishida in his experiments. The target was mounted inside a recovery box made of plywood and transparent plastic that had just a frontal aperture for the projectile and a lateral aperture for camera recordings. The entire set-up was then inserted into the collision chamber of the LGG for the tests. This method proved very effective since the debris cloud generated by the collisions was confined inside the recovery box. Moreover, the materials employed for the box were softer than aluminum and CFRPs, so we are sure that no deformation from secondary impacts occurred. After each hypervelocity collision the generated fragments were collected, weighed and cataloged in different size classes: $x > 3$ *mm* , 3 *mm* $\geq x > 2$ *mm* , 2 *mm* $\geq x > 1$ *mm* , 1 *mm* $\geq x > 0.5$ *mm* , and $x \leq 0.5$ *mm* .

2.3 Previous works

Using the same sets of fragments presented in this work, plus additional ones from other tests in the same experimental campaign, the CISAS researchers have already published several studies focused on the fragment distributions for aluminum [69] and CFRPs [73] separately. However, back then, debris were classified into size classes by manually sifting them through metallic meshes of different openings. The dimensions of the fragment were then measured using a custom MATLAB program starting from photographic scans of such fragments, while their masses were determined using a scale with 1 mg resolution. On that occasion, the analysis also assessed the efficiency of the process. By comparing the initial mass of the targets and the relative projectile with the mass of the damaged target after the impact plus the mass of the collected fragments, it was possible to evaluate the efficiency of mass collection (Table 2). Therefore, the mass collection efficiency is defined as follows:

$$\eta = \frac{M_{TARG,after} + m_{COLL}}{M_{TARG,before} + m_{PROJ}} \tag{2}$$

Test Code	***Target mass [g]***	***Projectile mass [g]***	***Target mass after impact [g]***	***Collected mass [g]***	***Lost mass [g]***	***Mass collection efficiency***
9225	*81.709*	*0.034*	*81.517*	*0.137*	*0.226*	*60.6%*
9235	*30.422*	*0.034*	*30.302*	*0.079*	*0.154*	*51.3%*
9222	*102.867*	*0.034*	*102.232*	*0.372*	*0.669*	*55.6%*
9234	*83.639*	*0.034*	*83.302*	*0.236*	*0.371*	*63.6%*

Table 2: Comparison of tests mass before and after the impact and relative mass collection efficiency

(a) Front

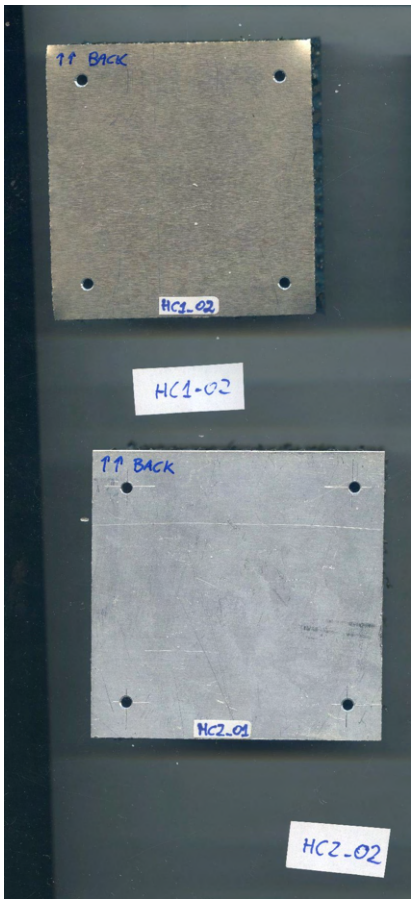

(b) Back

(c) Side

Figure 4: Images of the aluminum honeycomb targets in Test 9225 and in Test 9235 before the impact.

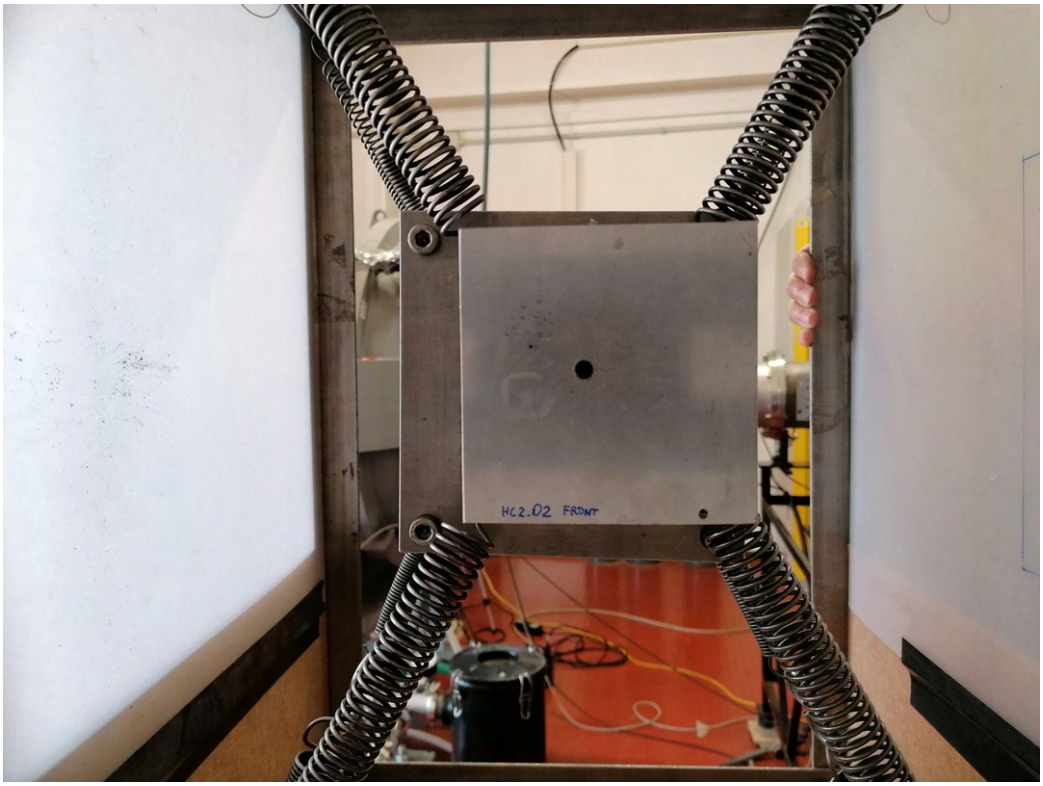

Figure 5: Target of Test 9225 after the impact.

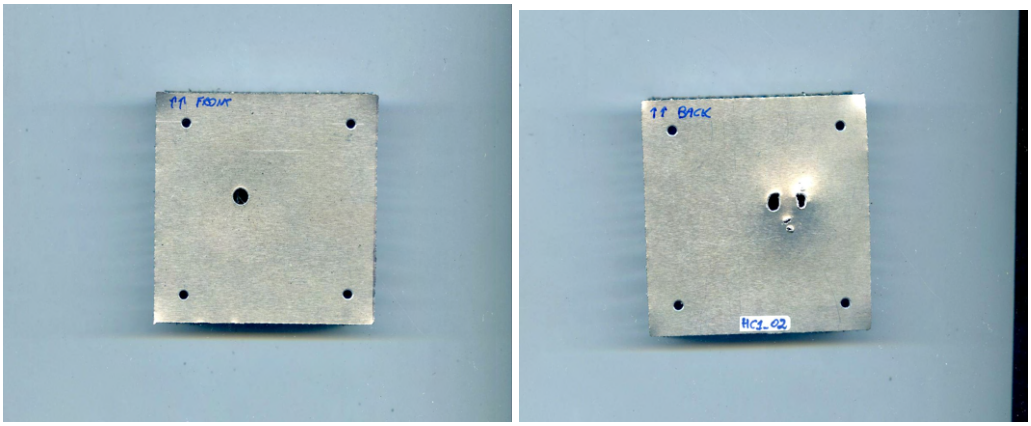

Figure 6: Target of Test 9235 after the impact. Front (left) and back (right).

Figure 7: Images of the CFRPs targets in Test 9222 (right side) and in Test 9234 (left side) before the impact.

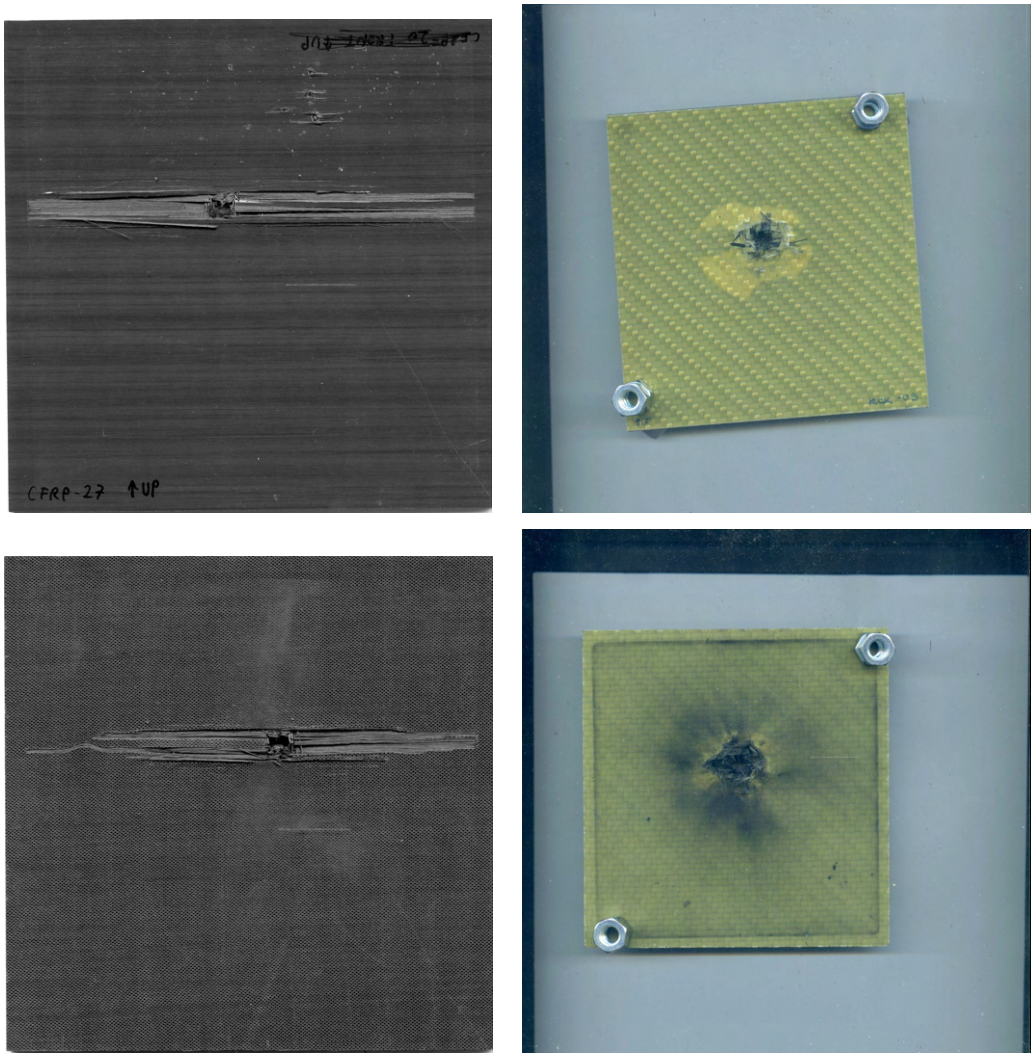

Figure 8: Images of the CFRPs targets in Test 9222 (right side) and in Test 9234 (left side) after the impact.

2.4 New analysis set-up and procedure

In this new work, the debris from the selected tests were re-analyzed with a different procedure and with a new goal. The entire data collection and analysis process was carried out at the CISAS Hypervelocity Impact Facility in Padova. Regarding the measurement instruments, the following instruments were available: a Mitutoyo Caliper having 0.01 *mm* resolution (Fig. 9b) and a KERN ADB Balance with 0.1 *mg* resolution (Fig. 9a) (Table 3).

	KERN ADB Balance	***Mitutoyo Caliper***
Resolution	0.0001 g	0.01 mm
Capacity	220 g	150 mm

Table 3: Specifications of the measurement instruments

For the analysis, the collected fragments of each test were positioned in a numbered grid, each of them was therefore identified by a unique number and individually cataloged. During this analysis, the following fragment parameters were collected: material, shape, three orthogonal dimensions, and weight. The data collection procedure for each fragment therefore included four main steps:

1. Visual identification of the material.
2. Visual classification of the shape.
3. Manual measurement of the three main orthogonal dimensions using the available digital caliper.
4. Weighting using the available scale.

The goal of this new work is to compare the fragment distributions of the two different materials.

(a) KERN ADB Balance

(b) Mitutoyo Caliper

Figure 9: Images of the measurement instruments adopted for the analysis

3 Results

After collecting the data, the analysis was performed using NASA's SBM formulations [50] to obtain the characteristic length and area-to-mass distributions. The results are then compared and discussed, with a focus also on the cumulative number and shape of the generated fragments in the four tests.

3.1 Fragments Shape

Firstly, we can consider the shape distributions of the debris resulting from the different tests. Fragments were classified into different shape classes by comparing their three orthogonal dimensions.

- Nuggets: irregular spheroids where the three main dimensions a, b and c are comparable.
- Cylinders: objects with an elongated shape where the three main dimensions a, b, c still have the same order of magnitude.
- Plates: objects with irregular planar geometry where the third dimension c is much smaller than the other two.
- Needles: needle-shaped objects where the larger dimension a is more than one order of magnitude greater than the other two.
- Wools: irregular agglomerates of fibers (present only in the Kevlar-reinforced samples)

We can observe that for aluminum honeycomb panels the debris generated by the impact are predominantly nuggets and plates, the latter probably resulting from the fragmentation of the internal honeycomb structure of the panels (Fig. 10). On the other hand, we can observe that debris coming from the CFRP plates mainly consist of needle-shaped objects resulting from the delamination of the plies of the composite plates (Fig. 10).
The difference in the shape distributions of the fragments confirms that the fragmentation process is heavily influenced by the mechanical behavior of the involved materials.
As expected, the anisotropic behavior of CFRP caused increased damage along the fiber direction due to the delamination process typical of composites. The anisotropy is also responsible for the large amount of needle-shaped fragments, which are instead totally absent in aluminum samples. In addition to the mechanical behavior of the main material, it can also be noted that the presence of a cover layer significantly affects the fragmentation process.

Comparing samples from the pure CFRP panel (Test 9222) and the Kevlar-reinforced one (Test 9234), the reinforcement layer caused a significant difference in the shape distribution of the fragments (Fig. 10) and surface damage (Fig. 8). In the simple CFRP target (Test 9222) the delamination process generated many needle-shaped fragments, some of which were as long as the plate itself. In contrast, in the kevlar-reinforced CFRP plate reinforced with kevlar (Test 9234), surface damage was much less evident and no large delaminated fragments were observed, indicating that the protective layer of Kevlar is effective in limiting surface delamination.

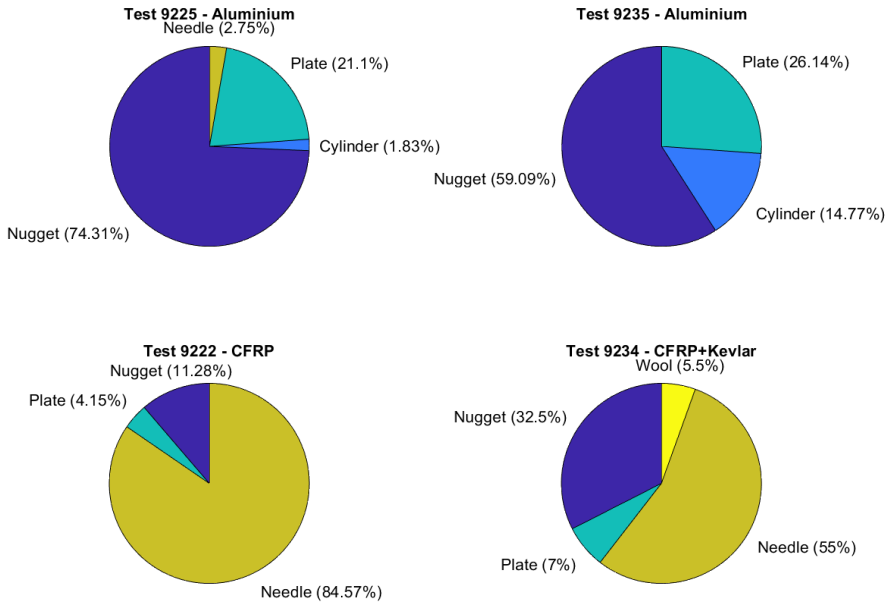

Figure 10: Comparison between the fragments shape distribution for aluminum honeycomb panels (above) and CFRPs (below).

3.2 Characteristic length distributions

In this subsection we take into account the characteristic length distributions of the collected fragments. The characteristic length Lc of an object is defined as the arithmetic mean of its three orthogonal dimensions a, b, and c :

$$L_c = \frac{a+b+c}{3} \tag{3}$$

From Fig. 11 it is evident how the materials affect both the number and the characteristic lengths of the fragments. Impact tests involving aluminum honeycomb panels show a similar trend in the characteristic length distribution and total number of fragments despite the different thicknesses of the targets and impact velocities in the two tests. From previous studies, it was found that the total number of fragments increases with impact velocity and decreases with thickness, meaning that thin targets generate more fragments than thicker ones [69]. These opposite effects are probably the reason for which we got a similar number of fragments even if the test conditions are different. Moving to impacts involving CFRPs, we can in general notice a higher number of fragments with respect to aluminum ones for the same impact velocities. Moreover, CFRP fragments tend to have larger characteristic lengths; this is mainly due to the large amount of needle-shaped objects.

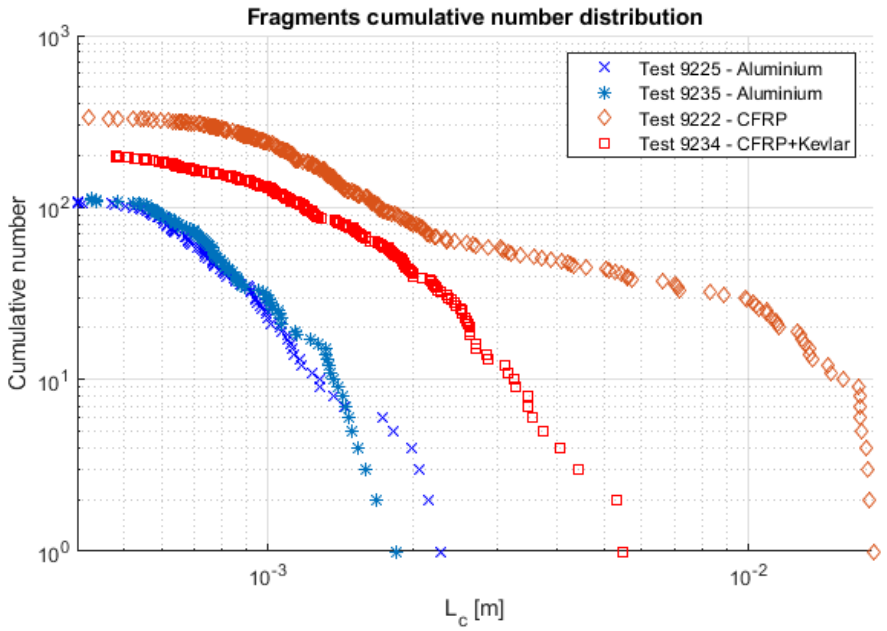

Figure 11: Fragments cumulative number distributions in function of their characteristic length.

An additional observation concerns the Kevlar-reinforced target. Since this target was thinner and the impact velocity of the test was higher, according to the trend previously identified, we could have expected more fragments than the pure CFRP target. Actually, the results show the opposite behavior, the Kevlar-reinforced target produced less fragments, even having smaller characteristic lengths. This behavior must therefore be related to the presence of the cover layer itself. Once again, we can conclude that the Kevlar reinforcement has a positive effect on the fragmentation process, limiting both the number of fragments and their sizes.

3.3 Fragments Mass

Here we examine the correlation between the mass of the fragments and their characteristic lengths. Plotting data in the logarithmic space, the average trend of the fragments mass distributions can be modeled by a least-squares fit lines: Fig. 12 and Fig. 13 show the fragment dataset, the least squares fit line (solid line) and the 1-σ deviation lines (dashed lines).
In general, as expected, we see that the mass increases with the size of the fragments, but irregular shapes cause a lot of deviation from this trend.
In addition to the equations of the best fit for each data set, the corresponding determination coefficient r^2 is also reported. The determination coefficient r^2 explains how well the regression line approximates the data, its value can range from 0 (no relations between the model and data variability) to 1 (perfect match between model and data, meaning that all points lie on the regression line). As we can see, the determination coefficient r^2 between the models and the data is positive but low. This suggests that the fitted models capture a general trend in the data, although significant scatter is present.
In the lower part of each graph, we can observe a lot of aligned points due to the sensitivity limit of the scale. Since a large number of fragments have masses close to this detection threshold and the instrument is unable to resolve small variations below it, an accumulation of data points occurs at the 0.1 *mg* and 0.2 *mg* scale readings. Having many fragments with the same mass spread over a wide range of characteristic length L_c is the main reason why the determination coefficient r^2 of the different fit models is low. This limitation could be overcome by using a scale with higher sensitivity, which was not available for the present study.

3.3.1 *m vs* L_c for tests on aluminum honeycomb panels

For tests conducted on aluminum honeycomb targets (Fig. 12) the best-fit for each dataset suggests the following relations:

$$\log_{10}(m) = 1.75 \log_{10}(L_c) - 1.10 \tag{4}$$

$$\log_{10}(m) = 1.69 \log_{10}(L_c) - 1.44 \tag{5}$$

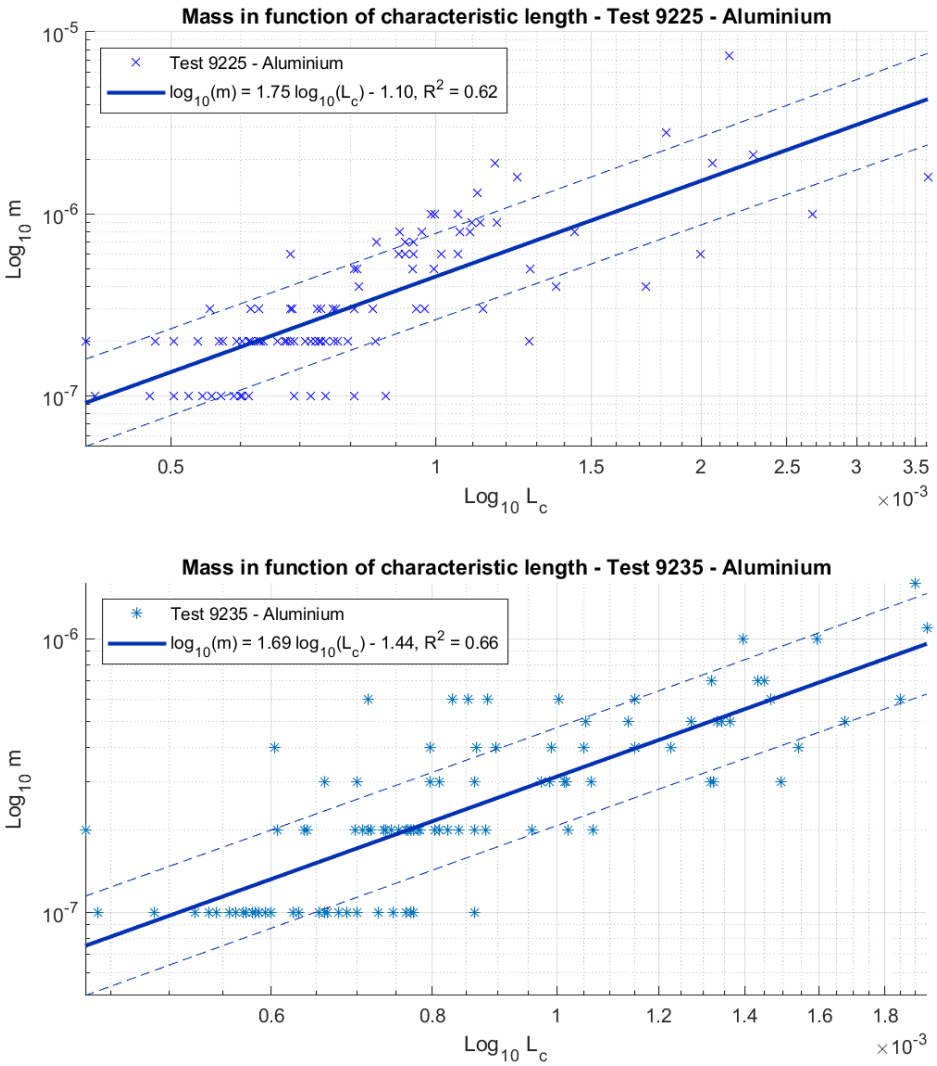

Figure 12: Fragments mass in function of characteristic length for samples coming from aluminum honeycomb panels impact tests.

3.3.2 *m vs* L_c for CFRPs

Meanwhile, considering the debris from composite targets (Fig. 13), the best-fit model for each test yields the following relationships:

$$\log_{10}(m) = 1.10 \log_{10}(L_c) - 3.38 \tag{6}$$

$$\log_{10}(m) = 1.17 \log_{10}(L_c) - 3.18 \tag{7}$$

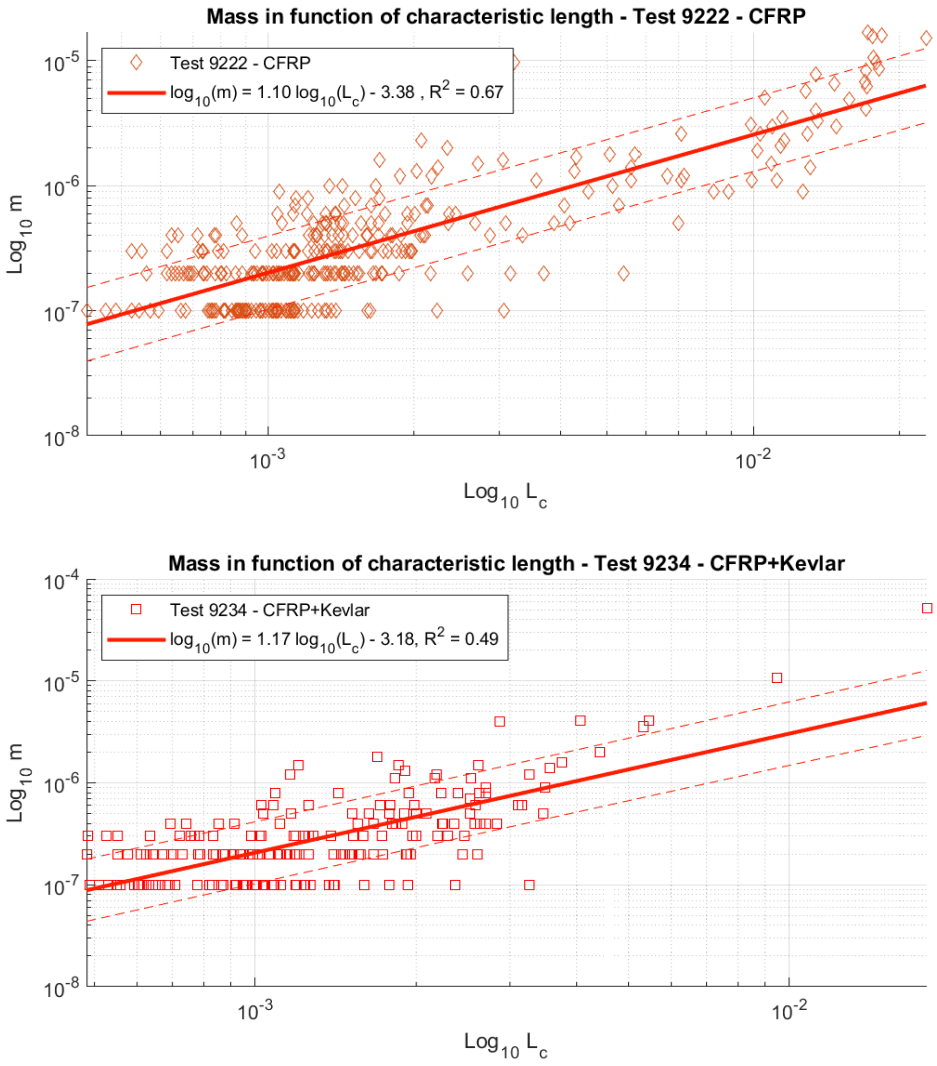

Figure 13: Fragments mass in function of characteristic length for samples coming from carbon-fiber-reinforced composite plates (CFRPs) impact tests.

3.3.3 *m vs* L_c : comparison between materials

Combining data from tests involving the same material, it was possible to obtain a representative linear trend for each material tested. Specifically, the average trend of the fragments mass distributions for aluminum is given by Eq. (8) while for composite it is given by Eq. (9).

$$\log_{10}(m) = 1.71 \log_{10}(L_c) - 1.29 \tag{8}$$

$$\log_{10}(m) = 1.11 \log_{10}(L_c) - 3.35 \tag{9}$$

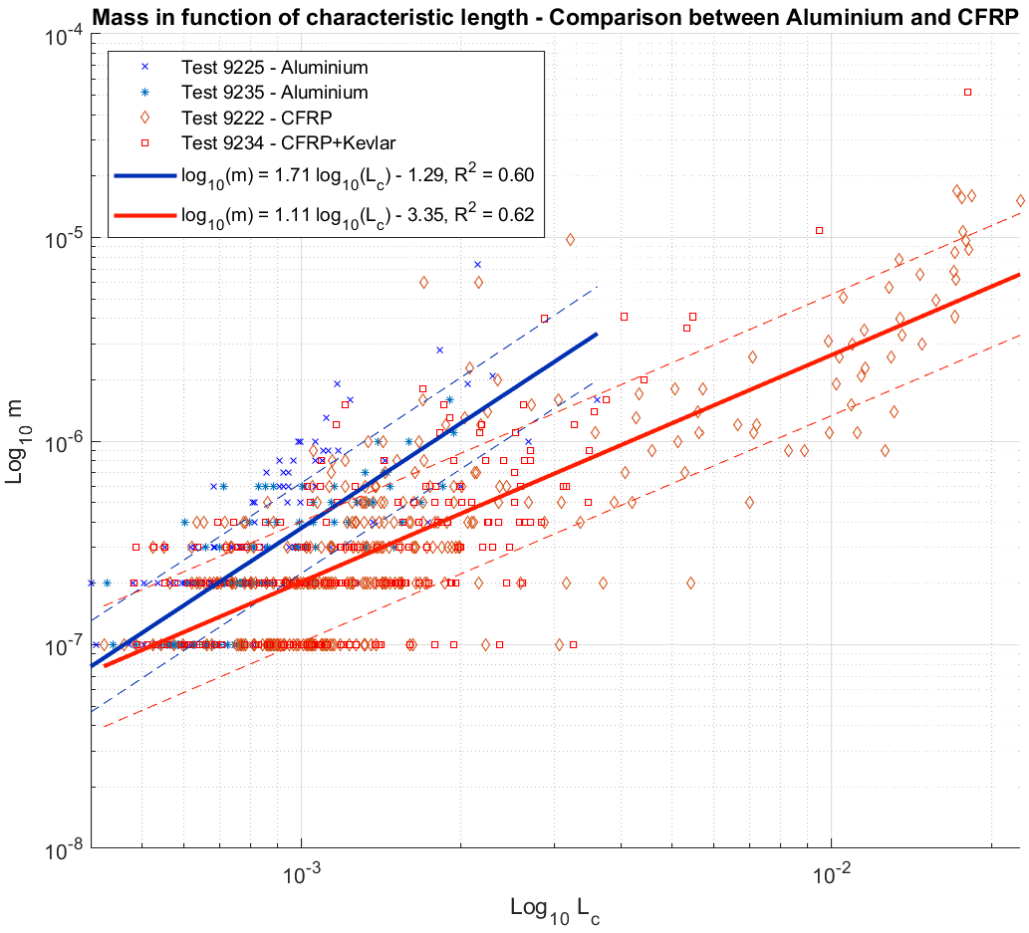

Figure 14: Fragments mass in function of characteristic length: comparison between samples coming from aluminum honeycomb panels impact tests and samples coming from carbon-fiber-reinforced composite plates (CFRPs) impact tests.

In Fig. 14, the trend lines for the two materials tested are shown together with the corresponding data points. We can see that the majority of the CFRP fragments (red squares and orange diamond marker) are below the aluminum ones (blue cross and light blue asterisk marker). This behavior is expected because carbon fibers have a lower density than aluminum. Comparing the trend lines for the two materials, for the same reason, we notice that the aluminum one present a higher angular coefficient (1.71) than the CFRP one (1.11).

Having a determination coefficient of 0.60 and 0.62 respectively, the trend lines for aluminum and CFRP fragments mass distribution provide reasonable approximations, yet a lot of variability is still present. However, if we consider the level of agreement between the general trend line of each material and those found in the corresponding individual tests, we obtain a very good agreement. This can be seen in Table 4 and Table 5 where the coefficient of determination r^2, the root mean square error RMSE and the bias (intended as the average logarithmic vertical shift) are compared.

	r^2	*RMSE*	*Bias*
Test 9225	0.9294	0.0790	0.0788
Test 9235	0.9063	0.0761	0.0760

Table 4: List of parameters values used to evaluate how well the linear model of the material for fragments mass in function of characteristic length agrees with the ones found for the two different impact tests on aluminum honeycomb panels.

	r^2	*RMSE*	*Bias*
Test 9222	0.9996	0.0081	0.0074
Test 9234	0.9961	0.0184	0.0143

Table 5: List of parameters values used to evaluate how well the linear model of the material for fragments mass in function of characteristic length agrees with the ones found for the two different impact tests on carbon-fiber-reinforced composite plates (CFRPs).

3.4 Area-to-mass ratio distributions

According to the NASA SBM formulation the cross sectional area A of the fragments is a function of the characteristic length L_c defined as:

$$A = 0.540424\ Lc^2 \qquad \text{if} \quad Lc < 0.00167\ m \tag{10}$$

$$A = 0.556945\ Lc^{2.047077} \qquad \text{if} \quad Lc \geq 0.00167\ m \tag{11}$$

The area-to-mass ratio (*A/m*) is obtained as the ratio between the cross-sectional area A and the mass m of the fragment. Studying the *A/m* distribution of fragments generated by impact events is important to evaluate the long-term evolution of the debris environment, since this parameter is directly related to the effect of perturbations (atmospheric drag and solar radiation pressure) on space debris [76, 77].

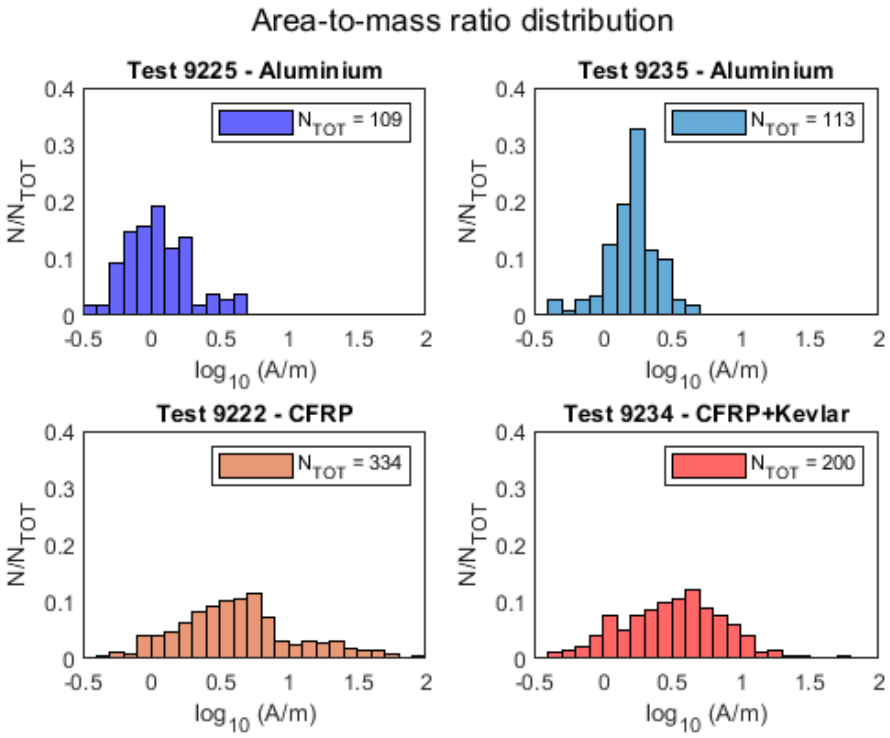

Figure 15: Area-to-mass ratio distribution for fragments coming from the different impact tests.

In Fig. 15 we can see the area-to-mass ratio distribution of the fragments resulting from the different impact tests. As we notice, aluminum debris are concentrated within a relatively narrow *A/m* range. In particular, Test 9225 shows

a peak at about 0.05 (corresponding to 1.12 m^2/kg), while Test 9235 shows a peak at approximately 0.25 (corresponding to 1.78 m^2/kg).
On the other hand, composite debris tend to be spread over a wider range of *A/m* values, with peaks located at a higher ratio with respect to aluminum. In fact, for Test 9222 and Test 9234 performed on CFRPs, the peaks occur at 0.75 (5.62 m^2/kg) and 0.65 (4.47 m^2/kg), respectively. Since both tests for each material exhibit consistent trends, we can conclude that the observed differences in the area-to-mass ratio distributions of the fragments are related to the different material properties. These results indicate that composite debris have larger *A/m* ratios than aluminum ones.

Then, a more accurate analysis on the *A/m* ratio distributions for the different impact tests was conducted, focusing on how these distributions change according to the size class of the fragments. Regardless of the material, Fig. 16 and Fig. 17 show that larger debris dimensions also correspond to higher *A/m* ratios. In fact, for each test analyzed, we see that the area-to-mass distributions progressively shift toward higher values as the fragment size class increases. Such behavior is well known for CFRPs fragments and is related to the predominant presence of needle-shaped objects. Meanwhile, this result is totally unexpected for aluminum. The main reason for these strange results is linked with the structural configuration of the targets, which were honeycomb panels and not simple aluminum plates. Tests on simple aluminum plates usually generate almost entirely irregular spheroids, here classified as nuggets. For this type of object, an increase in the size Lc results in an increase in area *A*, but the increase in volume is much more relevant. Through density, a drastic increase in volume translates into a rapid increase in mass *m*. In that case, A/m tends to decrease with size for this type of element, as pointed out in previous studies on aluminum plates.
The present studies instead involved honeycomb panels, which are very common in space applications. Consequently, fragments generated by the collision include a large number of plate objects coming from the internal structure of such panels. The area of a plate element rapidly increases with size, and the mass also increases proportionally; therefore, *A/m* ideally remains constant. The slight increase is justified by irregular shapes, which explains the observed shift.

A final consideration concerns the Kevlar reinforcement present in Test 9234. The presence of the reinforcement seems to not affect the peak of the area-to-mass distribution of the generated fragments but tends to affect the *A/m* range, limiting the upper tail of the distribution.

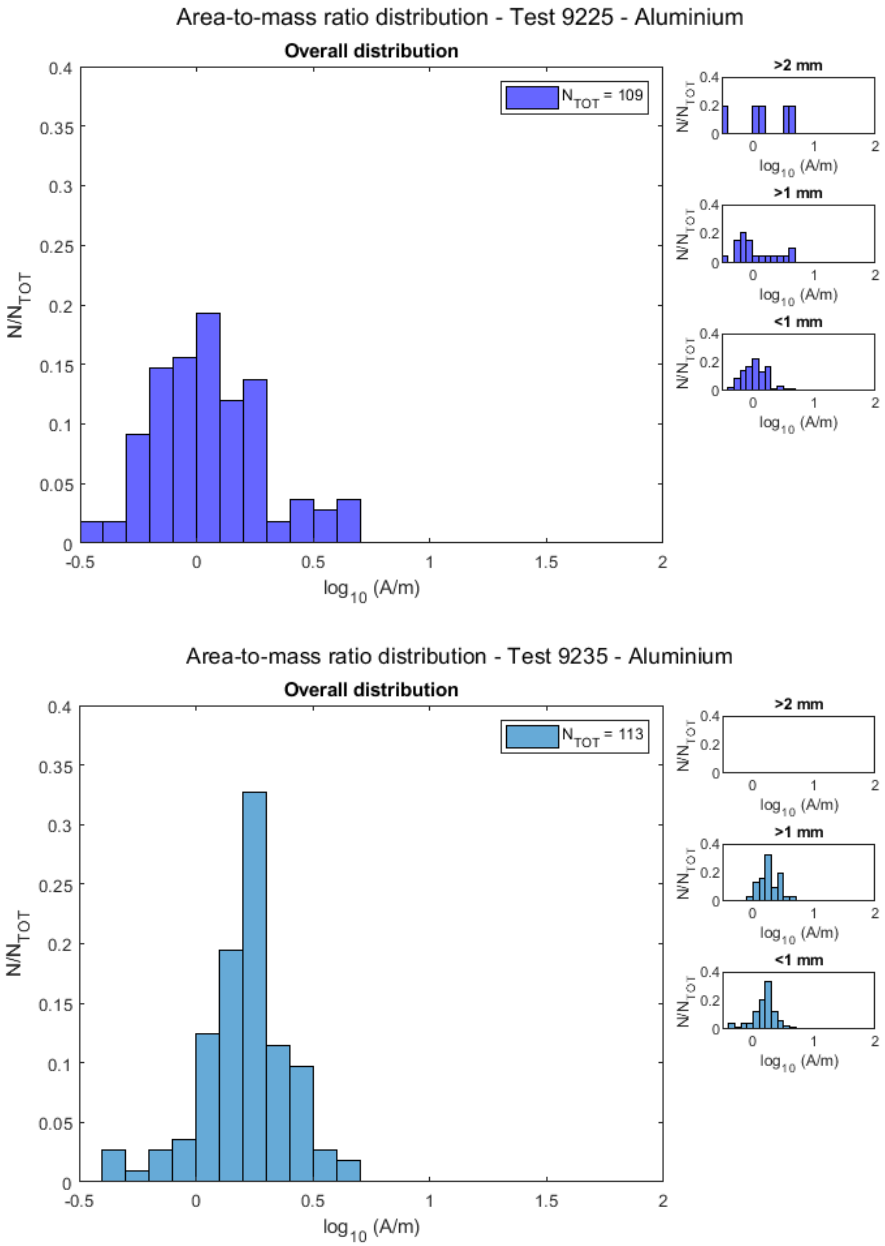

Figure 16: Area-to-mass ratio distribution for fragments coming from impact tests on aluminum honeycomb panels.

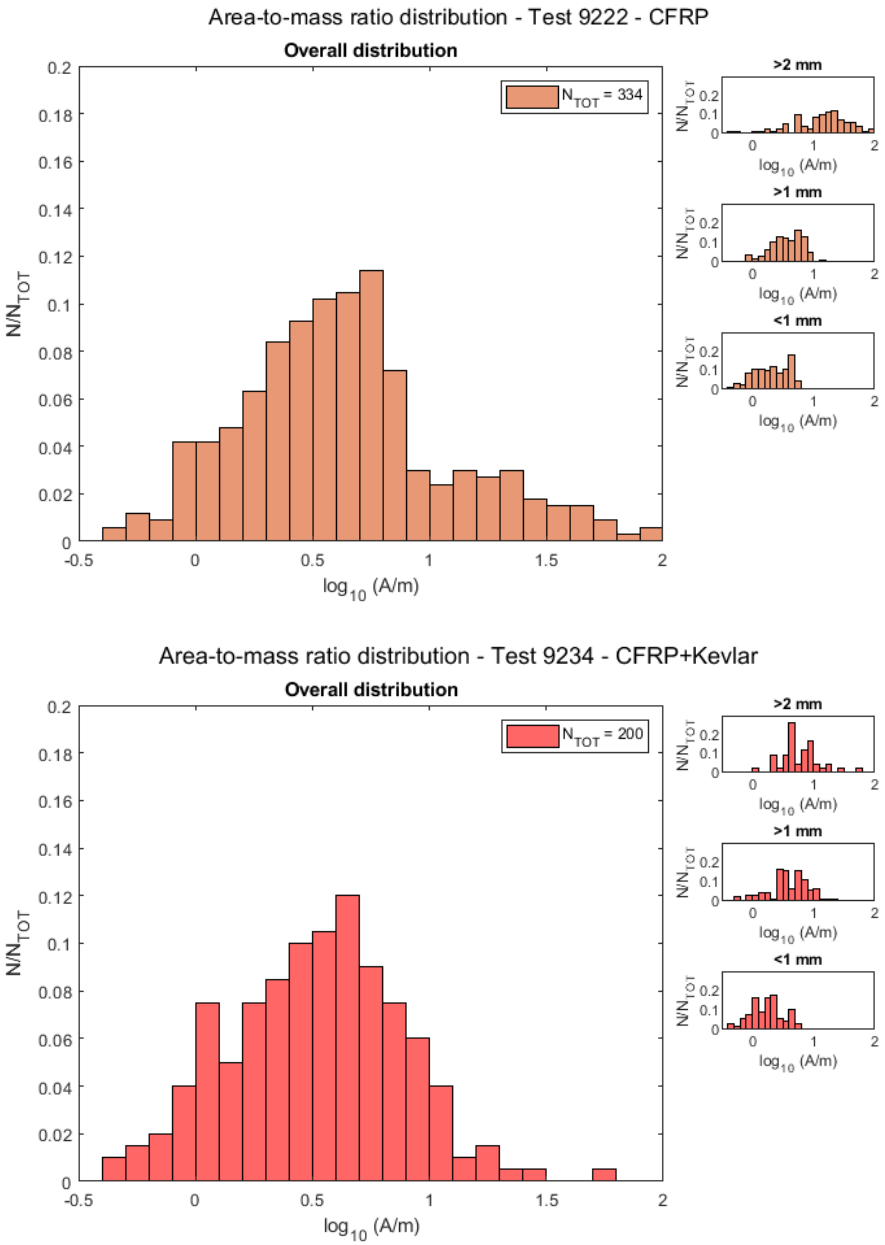

Figure 17: Area-to-mass ratio distribution for fragments coming from impact tests on carbon-fiber-reinforced composite plates (CFRPs).

3.5 Area-to-Mass Ratio versus Characteristic Length

The relationship between the area-to-mass ratio and the characteristic length is now examined to better underline how the size of the fragments affects the A/m ratio. In Fig. 18 and Fig. 21, test data are plotted in logarithmic space and the best-fit regression line is determined together with the relative determination coefficient.

3.5.1 *A/m vs* L_c for tests on aluminum honeycomb panels

For tests performed on aluminum honeycomb targets (Fig. 18), the following relations are obtained for the fragments of each test:

$$\log_{10}(A/m) = 0.25 \log_{10}(L_c) + 0.84 \tag{12}$$

$$\log_{10}(A/m) = 0.31 \log_{10}(L_c) + 1.17 \tag{13}$$

As pointed out in the previous section (3.4), for aluminum honeycomb panels, a general trend is observed suggesting that the larger the size of the fragment, the greater its area-to-mass ratio. However, the relations found are very weak and characterized by an extremely low coefficient of determination r^2. Nevertheless, the trend remains visible and consistent with the findings discussed in the previous section. The issue is not related to the model itself but to the data: the number of fragments analyzed was limited, and their characteristic lengths and mass were relatively similar. As a result, the plotted data resemble more clouds of points than linear distributions. Taking into account the difference in fragment shape, different relations could be obtained as shown in Fig. 19 and Fig. 20. In particular, as expected, it can be observed that the increase in *A/m* with size is mainly present for plate-shaped fragments, while it is absent or very small for nugget fragments. The conclusion is that the general trends found for the aluminum honeycomb tests are heavily affected by the presence of plate-shaped fragments.

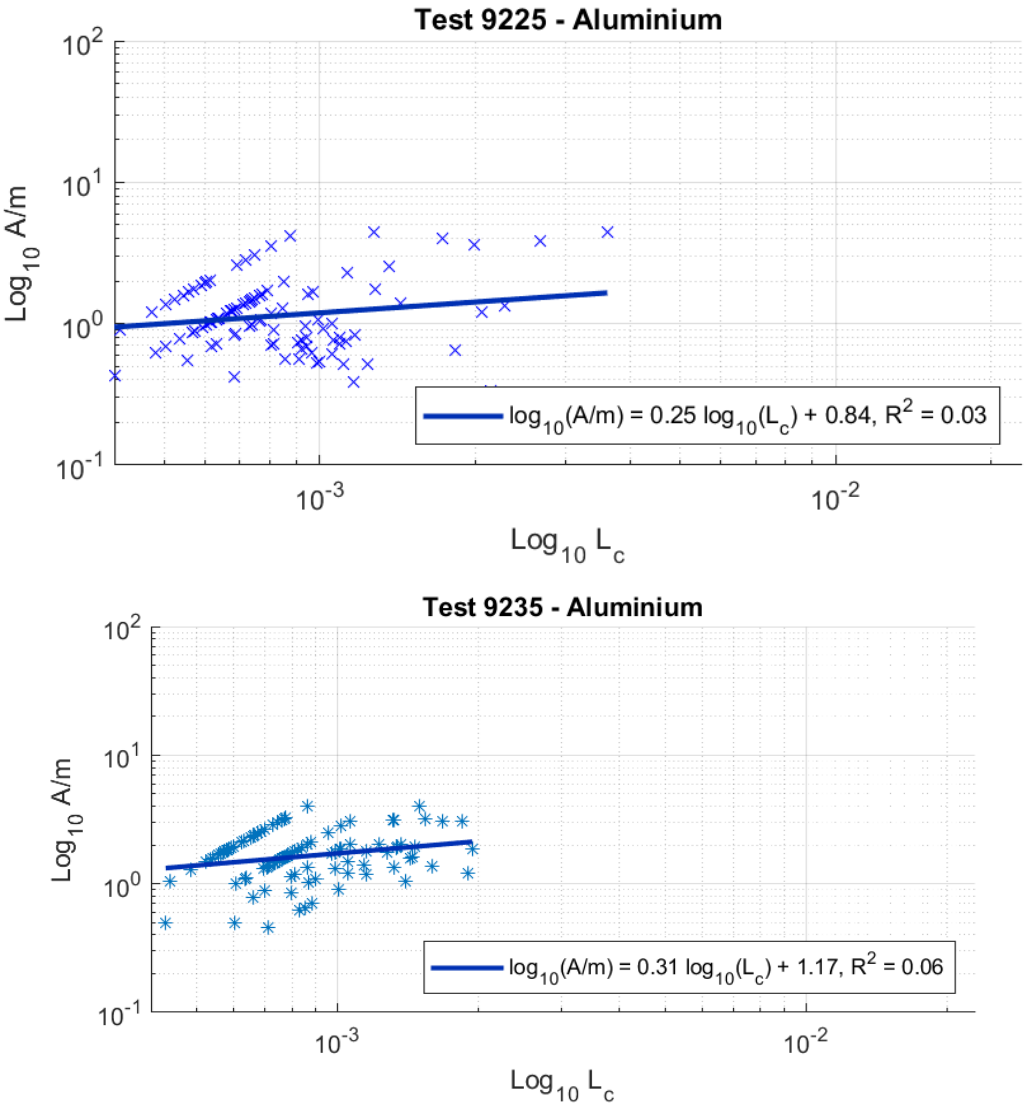

Figure 18: Area-to-mass ratio distribution versus characteristic length for fragments coming from impact tests on aluminum honeycomb panels.

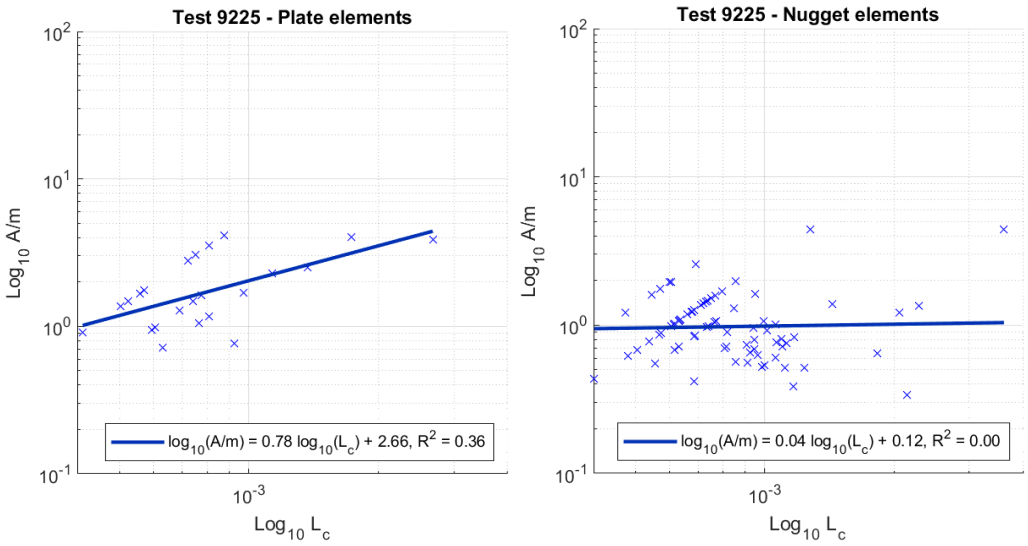

Figure 19: Comparison between area-to-mass ratio distribution versus characteristic length of plate fragments (on the left) and nugget fragments (on the right) of Test 9225.

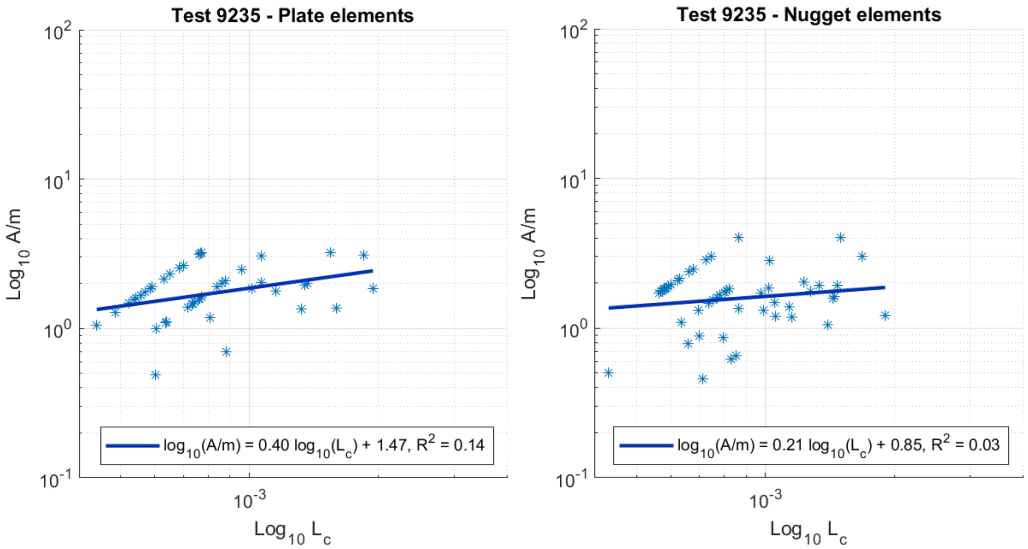

Figure 20: Comparison between area-to-mass ratio distribution versus characteristic length of plate fragments (on the left) and nugget fragments (on the right) of Test 9235.

3.5.2 *A/m vs* L_c for CFRPs

Meanwhile, for CFRP samples (Fig. 21), the best-fit model for each test provide:

$$\log_{10}(A/m) = 0.90 \log_{10}(L_c) + 3.12 \tag{14}$$

$$\log_{10}(A/m) = 0.83 \log_{10}(L_c) + 2.92 \tag{15}$$

Here, the same trend can also be observed in the data, meaning that the A/m ratio increases with the size of the fragment. In this case, the regression lines on both CFRP tests are characterized by a higher coefficient of determination r^2 compared to the aluminum ones. However, the same issue is still present for Test 9234, although less evident. This is due to the presence of Kevlar reinforcement; in fact, as discussed in Section 3.2, the main effect of such reinforcement is to limit the size of the fragments. Consequently, many fragments in this test are approximately the same size. The series of aligned points present in each plot again results from the sensitivity of the scale used for measurement. Since the scale has a sensitivity of 0.1 *mg*, it cannot resolve any difference below that threshold in the actual mass of the fragments. As a result, a lot of fragments are found to have a mass of 0.1 *mg* or 0.2 *mg*, as the instrument lacks sufficient precision to distinguish intermediate values.

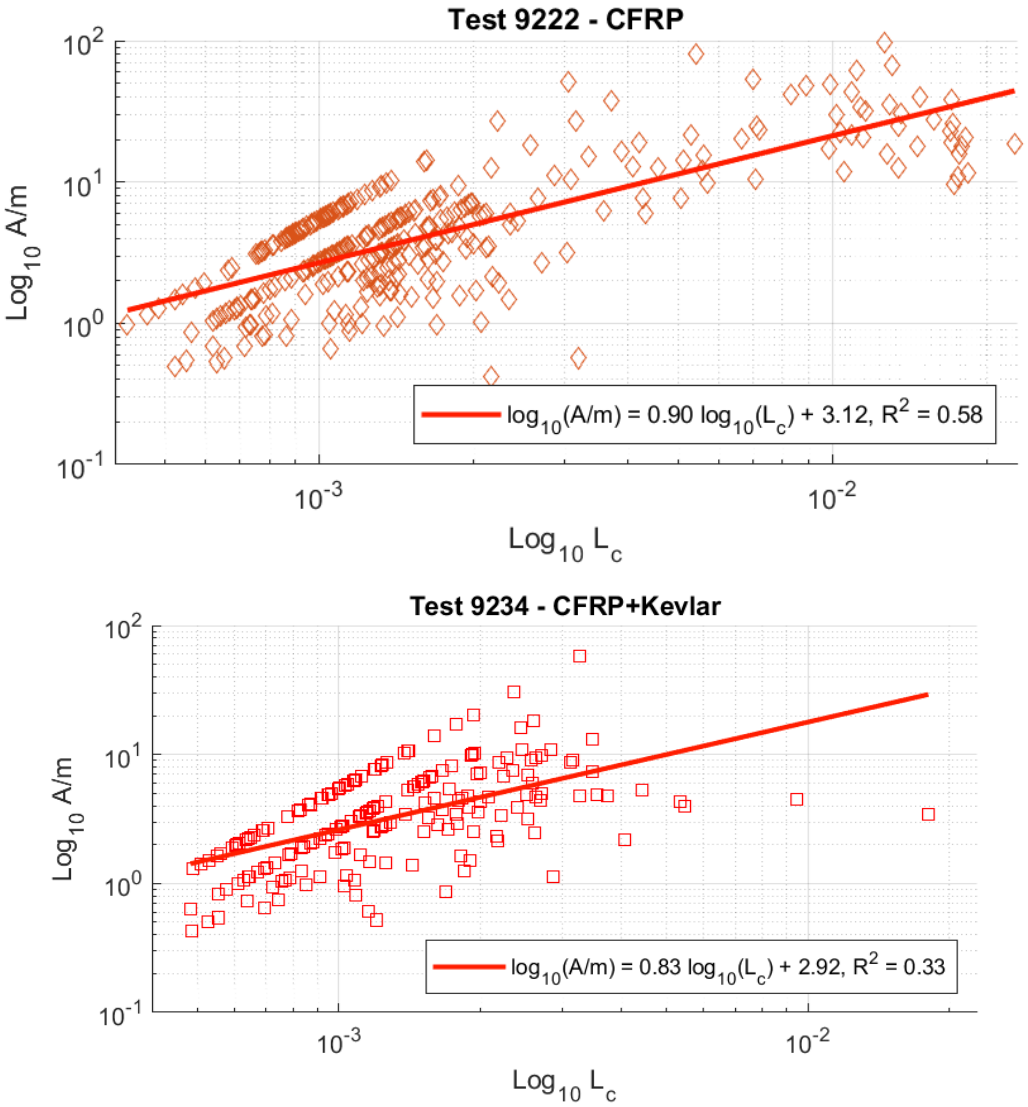

Figure 21: Area-to-mass ratio distribution versus characteristic length for fragments coming from impact tests on carbon-fiber-reinforced composite plates (CFRPs).

3.5.3 *A/m vs* L_c : comparison between materials

It is possible to develop a general law to describe the relationship between the area-to-mass ratio and the characteristic length for each material. By combining the two datasets collected for each material, the best linear regressions that fit all the data across these datasets can be determined. In that way, Eq. (16) is derived for fragments coming from aluminum honeycomb panels, while Eq. (17) is obtained for fragments from CFRPs.

$$\log_{10}(A/m) = 0.29 \log_{10}(L_c) + 1.03 \tag{16}$$

$$\log_{10}(A/m) = 0.89 \log_{10}(L_c) + 3.09 \tag{17}$$

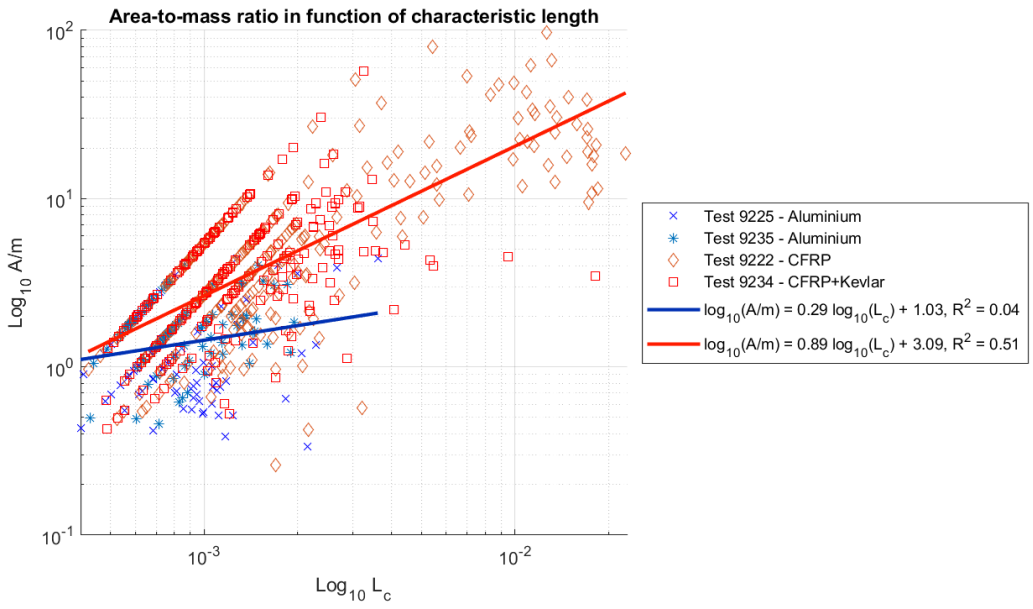

Figure 22: Area-to-mass ratio distribution versus characteristic length: comparison between aluminum and composite samples.

In Fig. 22, Eq. (16) for aluminum and Eq. (17) for CFRP are shown together with the corresponding datasets. It can be observed that the *A/m* tends to increase more rapidly with fragment size for composite materials, whereas this increment is way less evident for aluminum, as already pointed out when examining the individual tests. This behavior is also reflected by the angular coefficients of the regression lines found; in fact, the angular coefficient in Eq. (16) is just 0.29 compared to 0.89 of Eq. (17), so three times smaller.

Finally, the level of agreement between the general trend for each material and those obtained from the individual tests is evaluated. Again, this is studied considering the determination coefficient r^2, the root mean square error RMSE and the bias (Tables 6-7).

	r^2	***RMSE***	***Bias***
Test 9225	-2.3464	0.0790	0.0787
Test 9235	-1.7278	0.0760	0.0760

Table 6: List of parameters values used to evaluate how well the linear model of the material for area-to-mass ratio in function of characteristic length agrees with the ones found for the two different impact tests on aluminum honeycomb panels.

	r^2	***RMSE***	***Bias***
Test 9222	0.9994	0.0082	0.0074
Test 9234	0.9922	0.0186	0.0145

Table 7: List of parameters values used to evaluate how well the linear model of the material for area-to-mass ratio in function of characteristic length agrees with the ones found for the two different impact tests on carbon-fiber-reinforced composite plates (CFRPs).

Looking at Table 7, it can be seen that for the composite material, the agreement between the general trend and the individual tests is clearly evident from the high coefficient of determination values, which approach 1 in both cases. Furthermore, extremely low values of the RSME and bias consolidate the result. Regarding aluminum, the agreement is less apparent. As shown in Table 6, the r^2 values for each test are negative. Negative values of the coefficient of determination simply indicate that the mean value approximates the data better than the assumed regression model. In this case, this happens because the regression lines found for the individual tests and the one for the material are nearly parallel and have small angular coefficients, so they are almost horizontal. For this reason, r^2 is not always the best choice, and in many cases it is preferred to look at the RMSE or at the bias. Indeed, these values are very small for each case, proving that the general law found for aluminum is a very good approximation.

4 Conclusions

This thesis work consisted in analyzing the data collected from four fragmentation tests carried out at the Hypervelocity Impact Facility of the University of Padova. Two tests involved aluminum honeycomb panels, while the remaining two were conducted on carbon-fiber-reinforced composite plates (CFRPs). The fragments generated by these hypervelocity impact tests were manually measured and weighted using a caliper with a resolution of 0.01 *mm* and a scale with a resolution of 0.1 *mg*. In addition, fragments were characterized in terms of shape, which allowed the determination of the corresponding shape distributions for each test. The collected data were then used to derive the characteristic length cumulative distributions and the area-to-mass ratio using the NASA Standard Breakup Model. The comparison between the results of these tests on different types of targets shows that the fragment distributions are clearly affected by the target's material. For aluminum, which is an isotropic material, the damages on the targets were more uniform, and the sizes of the fragments were also more similar to each other. The fragments of the aluminum honeycomb panels consisted mainly of objects of irregular shapes with three comparable dimensions. In contrast, the anisotropic behavior of CFRP leads to more severe damage along the surface fiber direction, resulting in extensive delamination and large delaminated fragments. The number of fragments was significantly higher and consisted mainly of needle-shaped objects. Additionally, by comparing fragments from standard and Kevlar-reinforced composite plates, it can be observed that Kevlar reinforcement has a positive effect on the fragmentation process, limiting both the number of fragments and their sizes. The fragment mass increases with size independently of the material; however, the density of the material actually affects the trend of this relationship. For the same characteristic length, CFRP fragments generally exhibit lower masses than aluminum fragments. This is due to the fact that carbon fibers have lower density than aluminum. Comparing aluminum and composite *A/m* distributions, the former is concentrated around small *A/m* values, with a very sharp and well-defined peak, whereas the latter is distributed over a wider range, with a lower peak occurring at a higher *A/m* value. Anyway, it was observed that for larger fragments classes the area-to-mass ratio distribution shifts toward higher *A/m* values both for aluminum honeycomb panels and CFRPs. Although some limitations are present in this analysis, the results are consistent between different tests performed on the same type of target. Improvements of the results are possible by extending the analysis to further tests on both types of targets in order to consolidate the observed differences in the materials behavior. Repeating the measurements with a more precise scale with higher resolution would also enhance the accuracy of the results. The general conclusion of this

work is that materials and reinforcement cover layers, when present, play a significant role in the fragmentation process. As a future perspective, continuing to characterize the fragmentation behavior of different materials through further hypervelocity impact tests seems to be essential. In recent years, new materials have been developed and employed for the space sector thanks to advances in materials science and manufacturing technologies. Characterizing these new materials is crucial to understand the evolution of space debris expected to occur in the upcoming years.

References

[1] Adrian V Gheorghe and Daniel E Yuchnovicz. “The space infrastructure vulnerability cadastre: Orbital debris critical loads”. In: *International Journal of Disaster Risk Science* 6.4 (2015), pp. 359–371.

[2] IADC. *IADC Space Debris Mitigation Guidelines, Rev. 4,* tech. rep. January 2025. URL: https://www.iadc-home.org/documents_public/view/id/318#u.

[3] Phillip Anz-Meador, John Opiela, and Jer-Chyi Liou. *History of on-orbit satellite fragmentations*. Tech. rep. 2023.

[4] Luciano Anselmo, A Rossi, and C Pardini. “Updated results on the long-term evolution of the space debris environment”. In: *Advances in Space Research* 23.1 (1999), pp. 201–211.

[5] Alessandro Rossi et al. “Modelling the evolution of the space debris population”. In: *Planetary and Space Science* 46.11-12 (1998), pp. 1583–1596.

[6] Arif Goektug Karacalioglu and Jan Stupl. “The impact of new trends in satellite launches on the orbital debris environment”. In: *IAASS Conference aEurooeSafety First, Safety for AllaEuro*. ARC-E-DAA-TN31699. 2016.

[7] D McKnight et al. “Assessing potential for cross-contaminating breakup events from LEO to GEO”. In: *69th International Astronautical Congress. Presented Paper. Bremen, Germany*. 2018.

[8] Ritu S Lauer. “When states test their anti-satellite weapons”. In: *Astropolitics* 20.1 (2022), pp. 1–26.

[9] Carmen Pardini and Luciano Anselmo. “Assessment of the consequences of the Fengyun-1C breakup in low Earth orbit”. In: *Advances in Space Research* 44.5 (2009), pp. 545–557.

[10] James Murray et al. “Observations of Small Debris from the Cosmos 1408 Anti-Satellite Test using the HUSIR and Goldstone Radars”. In: *Advanced Maui Optical and Space Surveillance Technologies Conference (AMOS)*. 2022.

[11] Yu Jiang. “Debris cloud of India anti-satellite test to Microsat-R satellite”. In: *Heliyon* 6.8 (2020).

[12] Donald J Kessler. “Sources of orbital debris and the projected environment for future spacecraft”. In: *Journal of Spacecraft and Rockets* 18.4 (1981), pp. 357–360.

[13] Brian Tarran. “Prepare for impact: Space debris and statistics”. In: *Significance* 18.3 (2021), pp. 18–23.

[14] TS Kelso et al. “Analysis of the Iridium 33-Cosmos 2251 collision”. In: *Advances in the Astronautical Sciences* 135.2 (2009), pp. 1099–1112.

[15] Donald J Kessler and Burton G Cour-Palais. “Collision frequency of artificial satellites: The creation of a debris belt”. In: *Journal of Geophysical Research: Space Physics* 83.A6 (1978), pp. 2637–2646.

[16] Donald J Kessler et al. “The kessler syndrome: implications to future space operations”. In: *Advances in the Astronautical Sciences* 137.8 (2010), p. 2010.

[17] Nikita Bhakare. “The Need for Evolving Legal Framework for Regulation of Space Debris Caused by Satellite Constellations”. In: *Proceeding of 8th European Conference on Space Debris, the ESA Space Debris Office Ed. T. Flohrer, S. Lemmens & F. Schmitz*. 2021.

[18] Daniel L Oltrogge and Ian A Christensen. “Space governance in the new space era”. In: *Journal of Space Safety Engineering* 7.3 (2020), pp. 432–438.

[19] Jingrui Zhang et al. “Long-term evolution of the space environment considering constellation launches and debris disposal”. In: *IEEE Transactions on Aerospace and Electronic Systems* 59.5 (2023), pp. 6124–6137.

[20] Francesca Letizia, Benjamin Bastida Virgili, and Stijn Lemmens. “Assessment of orbital capacity thresholds through long-term simulations of the debris environment”. In: *Advances in Space Research* 72.7 (2023), pp. 2552–2569.

[21] Carmen Pardini and Luciano Anselmo. “Evaluating the impact of space activities in low earth orbit”. In: *Acta Astronautica* 184 (2021), pp. 11–22.

[22] Michael Swartwout. “University-Class Spacecraft in 2023: More Missions, More Problems?” In: (2023).

[23] Jonathan R Behrens and Bhavya Lal. “Exploring trends in the global small satellite ecosystem”. In: *New Space* 7.3 (2019), pp. 126–136.

[24] Erik Kulu. “Satellite constellations-2021 industry survey and trends”. In: (2021).

[25] Bettina Mrusek and Linda Weiland. “Space commercialization and the rise of constellations: The resulting impact on the kessler effect”. In: *2023 IEEE Aerospace Conference*. IEEE. 2023, pp. 01–07.

[26] Jennifer Alvarez and Buddy Walls. “Constellations, clusters, and communication technology: Expanding small satellite access to space”. In: *2016 IEEE aerospace conference*. IEEE. 2016, pp. 1–11.

[27] Lorenzo Olivieri and Alessandro Francesconi. “Large constellations assessment and optimization in LEO space debris environment”. In: *Advances in Space Research* 65.1 (2020), pp. 351–363.

[28] Carmen Pardini and Luciano Anselmo. “Environmental sustainability of large satellite constellations in low earth orbit”. In: *Acta Astronautica* 170 (2020), pp. 27–36.

[29] Veronica L Foreman, Afreen Siddiqi, and Olivier De Weck. “Large satellite constellation orbital debris impacts: Case studies of oneweb and spacex proposals”. In: *AIAA SPACE and Astronautics Forum and Exposition*. 2017, p. 5200.

[30] Luciano Anselmo and Carmen Pardini. “An index for ranking active debris removal targets in LEO”. In: *7th European Conference on Space Debris. ESA Space Debris Office, Darmstadt-ESOC*. 2017, pp. 18–21.

[31] Minghe Shan, Jian Guo, and Eberhard Gill. “Review and comparison of active space debris capturing and removal methods”. In: *Progress in aerospace sciences* 80 (2016), pp. 18–32.

[32] Pietro Tadini et al. “Active debris multi-removal mission concept based on hybrid propulsion”. In: *Acta Astronautica* 103 (2014), pp. 26–35.

[33] A Valmorbida et al. “Validation of enabling technologies for deorbiting devices based on electrodynamic tethers”. In: *Acta Astronautica* 198 (2022), pp. 707–719.

[34] Giacomo Muntoni et al. “Crowded space: A review on radar measurements for space debris monitoring and tracking”. In: *Applied Sciences* 11.4 (2021), p. 1364.

[35] Abid Murtaza et al. “Orbital debris threat for space sustainability and way forward”. In: *IEEE access* 8 (2020), pp. 61000–61019.

[36] Vitali Braun et al. “Recent developments in space debris environment modelling, verification and validation with MASTER”. In: *8th European Conference on Space Debris*. ESA Space Debris Office Darmstadt, Germany. 2021, p. 18.

[37] PH Krisko et al. “ORDEM 3.0 and MASTER-2009 modeled debris population comparison”. In: *Acta Astronautica* 113 (2015), pp. 204–211.

[38] Igor Molotov et al. “International scientific optical network for space debris research”. In: *Advances in Space Research* 41.7 (2008), pp. 1022–1028.

[39] James R Shell. “Optimizing orbital debris monitoring with optical telescopes”. In: (2010).

[40] Heiner Klinkrad. *Space debris: models and risk analysis*. Springer Science & Business Media, 2006.

[41] Eric L Christiansen. “Meteoroid/debris shielding (No. S-898)”. In: *Houston: National Aeronautics and Space Administration, Lyndon B. Johnson Space Center* (2003).

[42] EL Christiansen et al. “Enhanced meteoroid and orbital debris shielding”. In: *International Journal of Impact Engineering* 17.1-3 (1995), pp. 217–228.

[43] William P Schonberg, Alan J Bean, and Kent Darzi. *Hypervelocity impact physics*. Tech. rep. NASA, 1991.

[44] Gerhard Drolshagen. “Impact effects from small size meteoroids and space debris”. In: *Advances in space Research* 41.7 (2008), pp. 1123–1131.

[45] Eric L Christiansen and Justin H Kerr. “Ballistic limit equations for spacecraft shielding”. In: *International Journal of Impact Engineering* 26.1-10 (2001), pp. 93–104.

[46] Martin Schimmerohn et al. “Numerical investigation on the standard catastrophic breakup criteria”. In: *Acta Astronautica* 178 (2021), pp. 265–271.

[47] Alessandro Francesconi et al. “CST: A new semi-empirical tool for simulating spacecraft collisions in orbit”. In: *Acta Astronautica* 160 (2019), pp. 195–205.

[48] Juan C Dolado-Perez, Carmen Pardini, and Luciano Anselmo. “Review of uncertainty sources affecting the long-term predictions of space debris evolutionary models”. In: *Acta Astronautica* 113 (2015), pp. 51–65.

[49] LYNDON B JOHNSON SPACE CENTER. “NASA Standard Breakup Model 1998 Revision”. In: (1998).

[50] Nicholas L Johnson et al. “NASA’s new breakup model of EVOLVE 4.0”. In: *Advances in Space Research* 28.9 (2001), pp. 1377–1384.

[51] Stefano Lopresti et al. “Overview of Spacecraft-Fragmentation Testing”. In: *Aerotecnica Missili & Spazio* 103.4 (2024), pp. 391–399.

[52] L Olivieri and A Francesconi. “A novel size distribution model for debris generated by in-orbit collisions”. In: *International Journal of Impact Engineering* 199 (2025), p. 105246.

[53] Marlon Sorge, Glenn Peterson, and John McVey. “Forensic analysis of on-orbit debris generation events”. In: *7th ECSD, volume OTR* 513 (2017).

[54] EG Stansbery et al. “Characterization of the orbital debris environment from Haystack radar measurements”. In: *Advances in Space Research* 16.11 (1995), pp. 5–16.

[55] DS McKnight et al. “Satellite orbital debris characterization impact test (SOCIT) series data collection report”. In: *Kaman Sciences Corporation* (1995).

[56] DS McKnight et al. “Analysis of SOCIT debris data and correlation to NASA’s breakup models”. In: *Kaman Sciences Corporation* (1995).

[57] Toshiya Hanada et al. “Outcome of recent satellite impact experiments”. In: *Advances in Space Research* 44.5 (2009), pp. 558–567.

[58] Jer-Chyi Liou et al. “DebriSat-a planned laboratory-based satellite impact experiment for breakup fragment characterizations”. In: *6th European Conference on Space Debris*. JSC-CN-28456. 2013.

[59] T Hanada and J-C Liou. “Comparison of fragments created by low-and hyper-velocity impacts”. In: *Advances in Space Research* 41.7 (2008), pp. 1132–1137.

[60] Sheng-wei Lan et al. “Debris area distribution of spacecraft under hypervelocity impact”. In: *Acta Astronautica* 105.1 (2014), pp. 75–81.

[61] Hakim Abdulhamid et al. “On-ground HVI on a nanosatellite. Impact test, fragments recovery and characterization, impact simulations”. In: *Proceedings of the 8th ESA Space Debris Conference, Darmstadt, Germany*. Vol. 20. 2021.

[62] Lorenzo Olivieri, Cinzia Giacomuzzo, and Alessandro Francesconi. “Analysis of fragments larger than 2 mm generated by a picosatellite fragmentation experiment”. In: *Acta Astronautica* 204 (2023), pp. 418–424.

[63] S Lopresti et al. “Glancing Impact on a Picosatellte Mock-up: Test Results”. In: *Proceedings of the International Astronautical Congress, IAC*. Vol. 2023. International Astronautical Federation, IAF. 2023.

[64] PH Krisko, Matt Horstman, and ML Fudge. “SOCIT4 collisional-breakup test data analysis: With shape and materials characterization”. In: *Advances in Space Research* 41.7 (2008), pp. 1138–1146.

[65] Heather Cowardin et al. “Updates to the DebriSat project in support of improving breakup models and orbital debris risk assessments”. In: *Hypervelocity Impact Symposium*. Vol. 883556. American Society of Mechanical Engineers. 2019, V001T10A012.

[66] Masahiro Nishida et al. “Scaling laws for size distribution of fragments resulting from hypervelocity impacts of aluminum alloy spherical projectiles on thick aluminum alloy targets: Effects of impact velocity and projectile diameter”. In: *International Journal of Impact Engineering* 109 (2017), pp. 400–407.

[67] Masahiro Nishida, Koichi Hayashi, and Kazuki Toya. “Influence of impact angle on size distribution of fragments in hypervelocity impacts”. In: *International Journal of Impact Engineering* 128 (2019), pp. 86–93.

[68] Masahiro Nishida et al. “Influence of temperature on crater and ejecta size following hypervelocity impact of aluminum alloy spheres on thick aluminum alloy targets”. In: *International journal of impact engineering* 42 (2012), pp. 37–47.

[69] Lorenzo Olivieri, Cinzia Giacomuzzo, and Alessandro Francesconi. “Experimental fragments distributions for thin aluminium plates subjected to hypervelocity impacts”. In: *International Journal of Impact Engineering* 170 (2022), p. 104351.

[70] Emanuele A Slejko, Anna Gregorio, and Vanni Lughi. “Material selection for a CubeSat structural bus complying with debris mitigation”. In: *Advances in Space research* 67.5 (2021), pp. 1468–1476.

[71] Lorenzo Olivieri et al. “Experimental characterization of multi-layer 3D-printed shields for microsatellites”. In: *Journal of Space Safety Engineering* 7.2 (2020), pp. 125–136.

[72] Alessandro Francesconi et al. “Effects of high-speed impacts on CFRP plates for space applications”. In: *Advances in space research* 50.5 (2012), pp. 539–548.

[73] Lorenzo Olivieri, Cinzia Giacomuzzo, and Alessandro Francesconi. “Analysis of fragment distributions from carbon-fiber-reinforced composite panels subjected to hypervelocity impacts”. In: *AIAA Journal* 61.6 (2023), pp. 2702–2710.

[74] Masahiro Nishida et al. “Ejecta size distribution resulting from hypervelocity impact of spherical projectiles on CFRP laminates”. In: *Procedia Engineering* 58 (2013), pp. 533–542.

[75] S Lopresti et al. “Hypervelocity Impact Testing and Simulation at the University of Padova”. In: *Hypervelocity Impact Symposium*. Vol. 88728. American Society of Mechanical Engineers. 2024, V001T06A005.

[76] Luciano Anselmo and Carmen Pardini. “Long-term dynamical evolution of high area-to-mass ratio debris released into high earth orbits”. In: *Acta Astronautica* 67.1-2 (2010), pp. 204–216.

[77] SO Belkin and ED Kuznetsov. “Orbital flips due to solar radiation pressure for space debris in near-circular orbits”. In: *Acta Astronautica* 178 (2021), pp. 360–369.